



# Atomically Fe-doped $\text{MoS}_{2-x}$ with Fe-Mo dual sites for efficient electrocatalytic NO reduction to $\text{NH}_3$

Kai Chen<sup>a,1</sup>, Jiabin Wang<sup>a,1</sup>, Jilong Kang<sup>a</sup>, Xubin Lu<sup>a</sup>, Xiaolin Zhao<sup>b</sup>, Ke Chu<sup>a,\*</sup>

<sup>a</sup> School of Materials Science and Engineering, Lanzhou Jiaotong University, Lanzhou 730070, China

<sup>b</sup> National Engineering Laboratory for Electric Vehicles, Beijing Institute of Technology, Beijing 100081, China

## ARTICLE INFO

### Keywords:

Electrocatalytic NO-to- $\text{NH}_3$  conversion  
Atomic doping  
Vacancy engineering  
Theoretical computations

## ABSTRACT

Electrocatalytic NO-to- $\text{NH}_3$  conversion (NORR) provides an appealing route for both sustainable  $\text{NH}_3$  production and harmful NO abatement. Herein, we combine the strategies of atomic doping and vacancy engineering to design atomically Fe-doped and S-vacancy-rich  $\text{MoS}_2$  ( $\text{Fe}_1/\text{MoS}_{2-x}$ ) as a highly efficient NORR catalyst, showing the maximum  $\text{NH}_3$ -Faradaic efficiency of 82.5% and  $\text{NH}_3$  yield of  $288.2 \mu\text{mol h}^{-1} \text{cm}^{-2}$  at  $-0.6 \text{ V}$  vs. RHE. Theoretical calculations unveil that Fe-Mo dual sites created on  $\text{Fe}_1/\text{MoS}_{2-x}$  can cooperatively activate NO and dissociate the  $\text{N}=\text{O}$  bond, boost the protonation energetics and simultaneously suppress the competing hydrogen evolution, resulting in the significantly expedited NORR activity and selectivity.

## 1. Introduction

$\text{NH}_3$  is an important chemical for the production of nitrogenous fertilizer and also an ideal reproducible energy [1–3]. The industrial  $\text{NH}_3$  synthesis by Haber-Bosch process involves significant energy consumption and greenhouse gas emissions [4]. Ambient electrocatalytic  $\text{N}_2$ -to- $\text{NH}_3$  reduction (NRR) has received extensive attention as a green and energy-saving alternative to Haber-Bosch technology [5–13]. However, the NRR process suffers from extremely low  $\text{NH}_3$  yield rate and  $\text{NH}_3$ -Faradaic efficiencies ( $\text{FE}_{\text{NH}_3}$ ) due to the ultra-stable  $\text{N}=\text{N}$  bond and severe competing hydrogen evolution reaction (HER) [14]. Compared with  $\text{N}_2$ , NO has a lower dissociation energy of  $\text{N}=\text{O}$  bond [15–18], and thus electrocatalytic NO reduction to  $\text{NH}_3$  (NORR) is more attractive than NRR for  $\text{NH}_3$  electrosynthesis [19]. Meanwhile, NO is one of the major air pollutants and brings about the great harmful effects on the environment [20]. Thus, NORR provides an appealing route for both sustainable  $\text{NH}_3$  production and harmful NO abatement [21–23]. Nevertheless, NORR is still restricted by its complex reaction process and competing HER, and it is imminently desired to design high-performing catalysts to boost the NORR and impede the HER [24–35].

Mo functions as the active center in nitrogenases and a wide variety of Mo-based catalysts are investigated for the electroreduction of nitrogenous molecules into various value-added chemicals [2]. Among them,  $\text{MoS}_2$  has garnered the most interest because of its robust

capability to activate and dissociate the nitrogenous molecules, as well as other intriguing advantages of layered structure with large surface area, tunable electronic structure and high chemical stability. Recently, Sun and co-workers report that  $\text{MoS}_2$  is active for the NORR with the maximal  $\text{FE}_{\text{NH}_3}$  of 76.6% [17], promising the great potential of  $\text{MoS}_2$ -based catalysts for the NORR. Nevertheless, the NORR activity of pristine  $\text{MoS}_2$  is still unsatisfactory, due possibly to its catalytic inertness of basal planes as well as the limitation of active edges with high NO protonation barriers [17]. Vacancy engineering is known to be a powerful approach for the activation of basal planes to expose the active sites [36–39], while heteroatom doping can further regulate the active sites for optimizing the binding energies of reaction intermediates to decrease the energetic barriers [40–42]. In this regard, the combination of vacancy engineering and heteroatom doping is expected to further expedite the NORR activity of  $\text{MoS}_2$ .

Herein, inspired by the Fe as the crucial element of the catalysts for  $\text{NH}_3$  electrosynthesis [43–45], we combine the strategies of atomic Fe doping and vacancy engineering to regulate the electronic structures of  $\text{MoS}_2$  towards the enhanced NORR activity. The developed atomically Fe-doped and S-vacancy-rich  $\text{MoS}_2$  ( $\text{Fe}_1/\text{MoS}_{2-x}$ ) exhibits an excellent NORR performance which significantly surpasses that of the pristine  $\text{MoS}_2$  and most reported NORR catalysts. The underlying NORR mechanism of  $\text{Fe}_1/\text{MoS}_{2-x}$  is further theoretically unraveled by a combination of density functional theory (DFT) computations and molecular

\* Corresponding author.

E-mail address: [chuk630@mail.lzjtu.cn](mailto:chuk630@mail.lzjtu.cn) (K. Chu).

<sup>1</sup> These authors contributed equally to this work.

dynamics (MD) simulations.

## 2. Experimental section

$\text{Fe}_1/\text{MoS}_{2-x}$  was prepared by a facile one-step hydrothermal approach. Briefly, 1 mmol  $(\text{NH}_4)_6\text{Mo}_7\text{O}_{24} \cdot 4 \text{H}_2\text{O}$ , 30 mmol  $\text{CH}_4\text{N}_2\text{S}$ , and 0.175 mmol  $\text{Fe}_2(\text{SO}_4)_3 \cdot 9 \text{H}_2\text{O}$  were first dissolved in 35 mL deionized water under. The mixed solution was then hydrothermally treated at 220 °C for 18 h. After reaction, the products were collected by centrifugation and washed with deionized water and ethanol three times. Fe-free but S-vacancy-rich  $\text{MoS}_{2-x}$  was synthesized by the same procedure with  $\text{Fe}_1/\text{MoS}_{2-x}$  but without addition of  $\text{Fe}_2(\text{SO}_4)_3 \cdot 9 \text{H}_2\text{O}$ . Pristine  $\text{MoS}_2$  was prepared by the same procedure with  $\text{MoS}_{2-x}$  but changing the amount of  $\text{CH}_4\text{N}_2\text{S}$  to 14 mmol. The detailed information related to electrochemical measurements, characterizations and calculations are provided in the [supplementary materials](#).

## 3. Results and discussion

### 3.1. Characterizations of $\text{Fe}_1/\text{MoS}_{2-x}$

The XRD (Fig. 1a) pattern of  $\text{Fe}_1/\text{MoS}_{2-x}$  shows the characteristic peaks of 2 H- $\text{MoS}_2$ , while the Raman spectrum of  $\text{Fe}_1/\text{MoS}_{2-x}$  shows two characteristic  $A_1g$  and  $E_2g$  vibration peaks of  $\text{MoS}_2$  (Fig. S1), indicating that  $\text{Fe}_1/\text{MoS}_{2-x}$  retains the original structure of  $\text{MoS}_2$ . SEM (Fig. 1b) and TEM (Fig. 1c) images present the typical nanoflower morphology of  $\text{Fe}_1/\text{MoS}_{2-x}$ . The corresponding SAED pattern (Fig. 1c-inset) of  $\text{Fe}_1/\text{MoS}_{2-x}$  displays three diffraction rings corresponding to (002), (100), and (110) planes of 2 H- $\text{MoS}_2$ , in line with the XRD results (Fig. 1a). The HRTEM (Fig. 1d) image of  $\text{Fe}_1/\text{MoS}_{2-x}$  reveals a widened interlayer spacing of 0.65 nm compared to pristine  $\text{MoS}_2$  (0.62 nm), caused primarily by the surface defects, i.e., S-vacancy ( $V_S$ ) [46]. The inverse fast Fourier transform (IFFT) images taken from the marked e, f areas of Fig. 1d show the distinct lattice distortions (green circles) on both edges (Fig. 1e) and basal planes (Fig. 1f), confirming the rich surface defects involved in  $\text{Fe}_1/\text{MoS}_{2-x}$  [46]. These defects can simultaneously introduce significant strains, as evidenced by the basal-plane geometric phase analysis (GPA, Fig. 1g). The element mapping images (Fig. 1h) verify a homogeneous distribution of Fe-dopants on  $\text{Fe}_1/\text{MoS}_{2-x}$ . The Fe content is determined to be 4.38 wt% by inductively coupled plasma spectroscopy.

The XPS-Fe2p spectra of  $\text{Fe}_1/\text{MoS}_{2-x}$  (Fig. 2a) show the distinct peaks assigned to Fe-S bond, which are absent for pristine  $\text{MoS}_2$  [47–49]. Both  $\text{MoS}_2$  and  $\text{Fe}_1/\text{MoS}_{2-x}$  show the similar deconvoluted Mo3d (Fig. 2b) and S2p (Fig. 2c) spectra [48], whereas the core-level Mo3d<sub>5/2</sub> and S2p<sub>3/2</sub> peaks of  $\text{Fe}_1/\text{MoS}_{2-x}$  are both positively shifted relative to  $\text{MoS}_2$ , suggesting the increased Mo and S valence states of  $\text{Fe}_1/\text{MoS}_{2-x}$  [50]. In addition, due to the existence of Fe-dopants, doublet peaks related to Fe-S bond emerge in the S2p spectra of  $\text{Fe}_1/\text{MoS}_{2-x}$  (Fig. 2c).

The XPS-Fe2p spectra of  $\text{Fe}_1/\text{MoS}_{2-x}$  (Fig. 2a) show the distinct peaks assigned to Fe-S bond, which are absent for pristine  $\text{MoS}_2$  [47–49]. Both  $\text{MoS}_2$  and  $\text{Fe}_1/\text{MoS}_{2-x}$  show the similar deconvoluted Mo3d (Fig. 2b) and S2p (Fig. 2c) spectra [48], whereas the core-level Mo3d<sub>5/2</sub> and S2p<sub>3/2</sub> peaks of  $\text{Fe}_1/\text{MoS}_{2-x}$  are both positively shifted relative to  $\text{MoS}_2$ , suggesting the increased Mo and S valence states of  $\text{Fe}_1/\text{MoS}_{2-x}$  [50]. In addition, due to the existence of Fe-dopants, doublet peaks related to Fe-S bond emerge in the S2p spectra of  $\text{Fe}_1/\text{MoS}_{2-x}$  (Fig. 2c).

Fig. 2d shows Fe K-edge XANES spectra of  $\text{Fe}_1/\text{MoS}_{2-x}$  and three reference samples of Fe foil, FeO and  $\text{Fe}_2\text{O}_3$ . Visibly, the absorption edge of  $\text{Fe}_1/\text{MoS}_{2-x}$  is between FeO and  $\text{Fe}_2\text{O}_3$ , indicating that Fe-dopants are positively charged between 2+ and 3+. The EXAFS spectra (Fig. 2e) of  $\text{Fe}_1/\text{MoS}_{2-x}$  present only one peak at 1.8 Å, corresponding to the nearest shell coordination of Fe-S bond [47,51], confirming the atomically

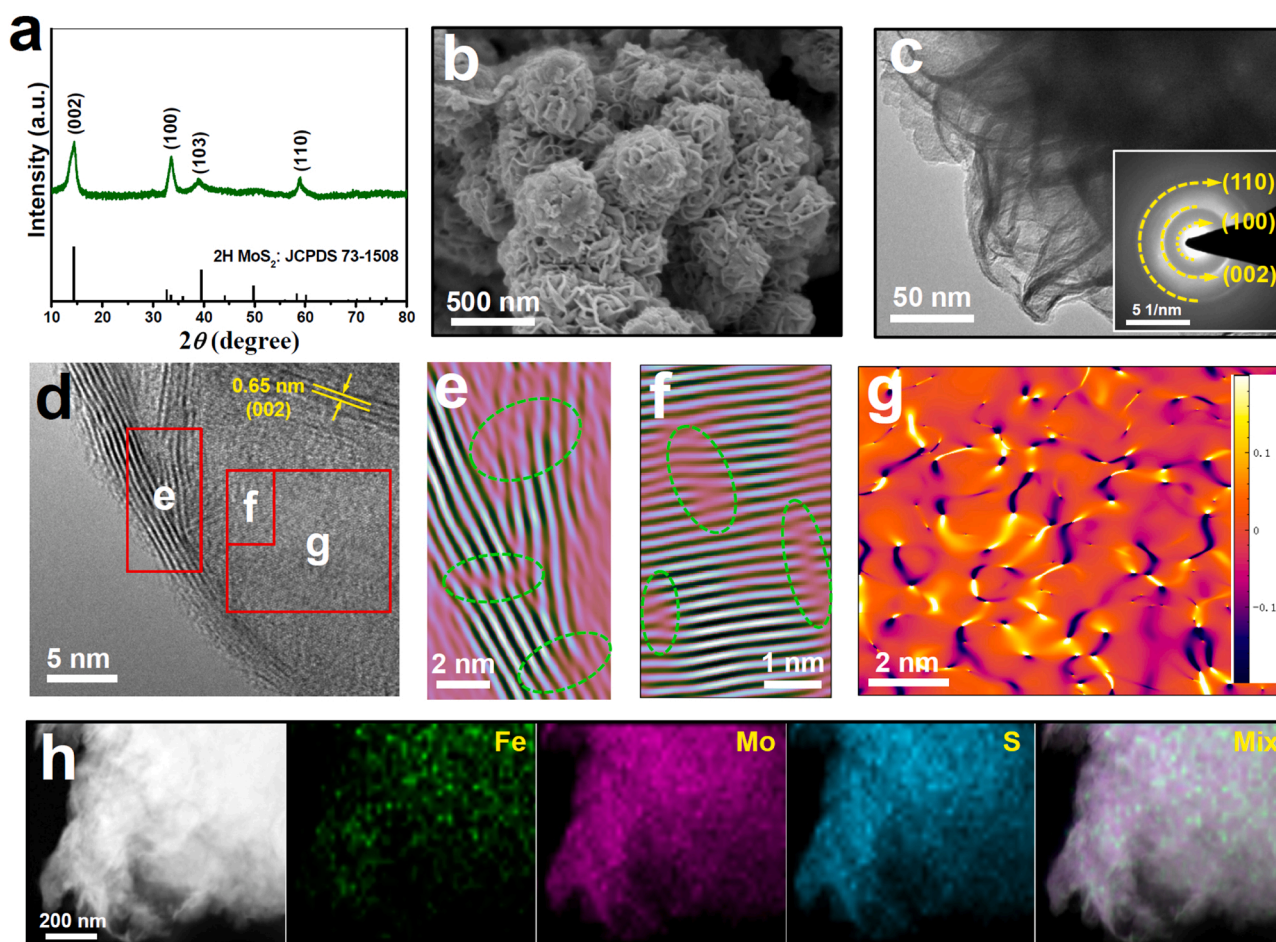


**Fig. 1.** Characterizations of  $\text{Fe}_1/\text{MoS}_{2-x}$ : (a) XRD pattern, (b) SEM image, (c) TEM image (inset: SAED pattern), (d) HRTEM image and corresponding (e, f) IFFT and (g) GPA image. (h) Element mapping images.

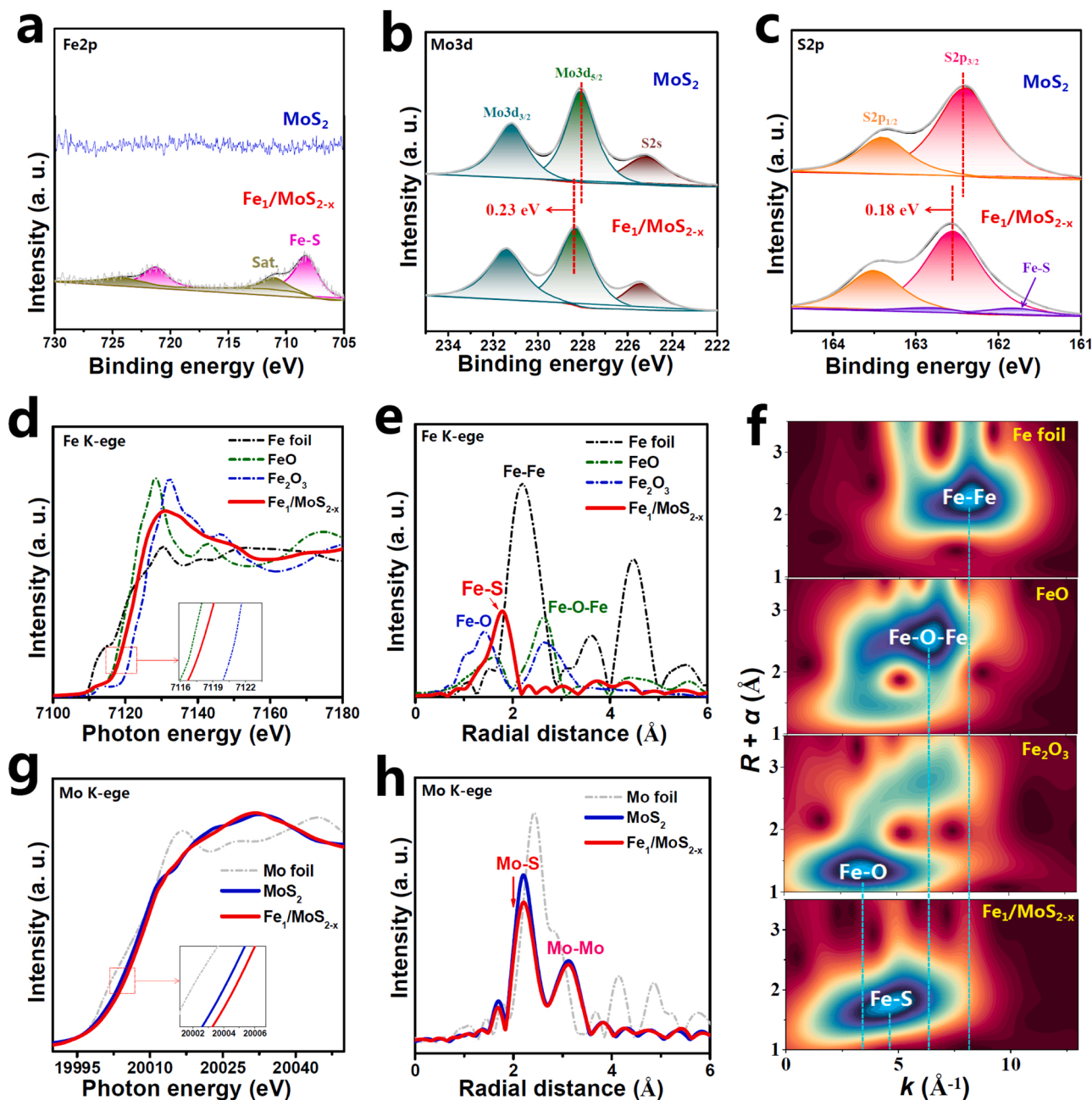


**Fig. 2.** (a–c) XPS spectra of  $\text{MoS}_2$  and  $\text{Fe}_1/\text{MoS}_{2-x}$ : (a) Fe2p, (b) Mo3d, (c) S2p. (d) Fe K-edge XANES, (e) EXAFS spectra and (f) WT profiles of  $\text{Fe}_1/\text{MoS}_{2-x}$  and reference samples of Fe foil, FeO and  $\text{Fe}_2\text{O}_3$ . (g) Mo K-edge XANES and (h) EXAFS spectra of Mo foil,  $\text{MoS}_2$  and  $\text{Fe}_1/\text{MoS}_{2-x}$ .

dispersed Fe dopants that are coordinated with the lattice S atoms. Likewise, the corresponding wavelet transform (WT, Fig. 2f) contour plots display a sole intensity maximum at  $4.6 \text{ \AA}^{-1}$  assigned to the Fe-S coordination which differs from Fe-Fe, Fe-O and Fe-O-Fe coordination bonds, further attesting the atomic-level distribution of Fe-dopants [52–55]. The least-squares EXAFS fitting analysis (Fig. S2, Table S1) reveals the coordination number of Fe-S coordination being around 5, identifying that Fe-dopants mainly substitute the five-fold unsaturated coordinated Mo atoms nearby the  $\text{V}_\text{S}$  in  $\text{MoS}_{2-x}$  (Fig. S2, inset). The Mo K-edge XANES spectra of  $\text{Fe}_1/\text{MoS}_{2-x}$  (Fig. 2g) show a positive shift of absorption edge relative to  $\text{MoS}_2$ , implying the increased Mo valence state of  $\text{Fe}_1/\text{MoS}_{2-x}$ , in line with the XPS analysis (Fig. 2b). In the Mo K-edge EXAFS spectra (Fig. 2h), compared to pristine  $\text{MoS}_2$ ,  $\text{Fe}_1/\text{MoS}_{2-x}$  exhibits a remarkably damped Mo-S bond intensity, while its Mo-Mo bond intensity remains almost the same, suggesting the decreased

number of Mo-S bonds and thus there exists abundant  $\text{V}_\text{S}$  in  $\text{Fe}_1/\text{MoS}_{2-x}$ . The enriched  $\text{V}_\text{S}$  in  $\text{Fe}_1/\text{MoS}_{2-x}$  can be further evidenced by the EPR spectra (Fig. S3) [56,57], showing that  $\text{Fe}_1/\text{MoS}_{2-x}$  displays a much stronger g signal at 2.003 than pristine  $\text{MoS}_2$ .

### 3.2. Electronic structure analysis and MD simulations

Generally, direct substitution of Mo atoms by Fe-dopants ( $\text{Fe}_1/\text{MoS}_2$ ) requires a high energy input (Fe-dopant formation energy  $E_\text{Fe} = 2.36 \text{ eV}$ , Fig. 3a), and thus is thermodynamically unfavorable. Upon introducing  $\text{V}_\text{S}$ , however,  $E_\text{Fe}$  becomes negative ( $E_\text{Fe} = -0.79 \text{ eV}$ , Fig. 3b), which means that Fe-doping of  $\text{MoS}_2$  would be thermodynamically feasible in the presence of  $\text{V}_\text{S}$ . Hence,  $\text{V}_\text{S}$  is essential for achieving the high concentration of Fe-dopants in  $\text{Fe}_1/\text{MoS}_{2-x}$ . In addition, the ab initio molecular dynamic (AIMD, Fig. 3c) simulations reveal the equilibrium



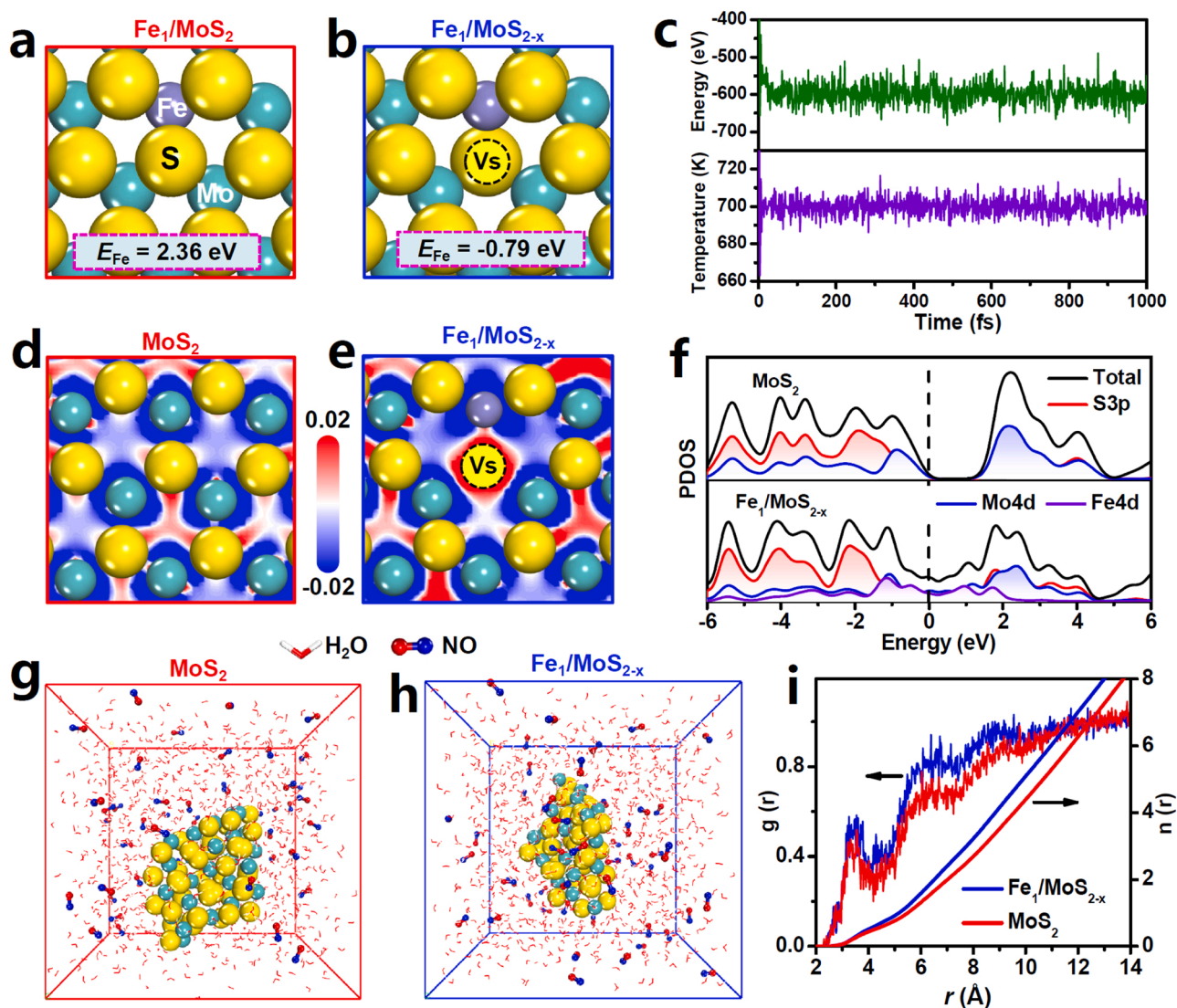


**Fig. 3.** (a, b) Calculated  $E_{Fe}$  of (a) Fe<sub>1</sub>/MoS<sub>2</sub> and (b) Fe<sub>1</sub>/MoS<sub>2-x</sub>. (c) Energy and temperature variations during the AIMD simulation for 1000 fs. (d, e) Electron contour maps of (d) MoS<sub>2</sub> and (e) Fe<sub>1</sub>/MoS<sub>2-x</sub> sliced along (001) plane. Blue and red regions represent electron depletion and accumulation, respectively. (f) PDOS of MoS<sub>2</sub> and Fe<sub>1</sub>/MoS<sub>2-x</sub>. (g, h) Snapshots for the dynamic process of NO adsorption on MoS<sub>2</sub> and Fe<sub>1</sub>/MoS<sub>2-x</sub> after MD simulations, and corresponding (i) radial distribution function (RDF, left) and integrated RDF (right) curves.

temperature and energy state under 700 K, confirming the robust stability of Fe<sub>1</sub>/MoS<sub>2-x</sub> configuration where Fe-dopants and V<sub>s</sub> can thermodynamically coexist.

The electron contour maps show that compared to MoS<sub>2</sub> (Fig. 3d), Fe<sub>1</sub>/MoS<sub>2-x</sub> (Fig. 3e) shows an obvious electron accumulation around V<sub>s</sub> while depletion around unsaturated-Mo and Fe-dopant. This phenomenon is also clearly reflected by the charge density difference plots and detailed charge analysis (Fig. S4). These electron-deficient Mo and Fe sites can serve as Lewis acid sites to not only enhance the adsorption and activation of Lewis-base NO during the NORR process, but also impede the binding of positively-charged protons, thus facilitating both NORR activity and selectivity. Projected density of states (PDOS, Fig. 3f) profiles show that pristine MoS<sub>2</sub> presents a semiconductor nature with an obvious band gap, while Fe<sub>1</sub>/MoS<sub>2-x</sub> shows the distinct electronic states crossing the Fermi level, which fully occupy the band gap and improves the conductivity. The enhanced conductivity of Fe<sub>1</sub>/MoS<sub>2-x</sub> is also confirmed by its reduced work function compared to MoS<sub>2</sub> (Fig. S5). Consequently, the introduction of both Fe-dopant and V<sub>s</sub> can jointly improve the conductivity of Fe<sub>1</sub>/MoS<sub>2-x</sub>, which facilitates the accelerated electron transport and boosted NORR reaction kinetics.

We perform the MD simulations to preliminarily examine the NORR activity of Fe<sub>1</sub>/MoS<sub>2-x</sub> (Fig. S6). After the simulations, the snapshots display more NO coverage on Fe<sub>1</sub>/MoS<sub>2-x</sub> (Fig. 3h) surface compared to that on MoS<sub>2</sub> (Fig. 3g). The corresponding RDF curves (Fig. 3i) reveal an enhanced NO-Fe<sub>1</sub>/MoS<sub>2-x</sub> interactions relative to MoS<sub>2</sub>, which is in line with the integrated RDF curves and confirms the enhanced NO affinity to Fe<sub>1</sub>/MoS<sub>2-x</sub>. Therefore, the introduced V<sub>s</sub> and Fe-dopants endow FeMoS<sub>2-x</sub> with the enhanced NO enrichment and coverage, which is beneficial to the NO supply toward the active sites and greatly promote the NORR process [58].

### 3.3. Electrocatalytic NORR performance

Electrocatalytic NORR performance of Fe<sub>1</sub>/MoS<sub>2-x</sub> is evaluated in a gas-tight electrochemical H-cell containing 0.5 M Na<sub>2</sub>SO<sub>4</sub> [17]. The ion chromatography (IC, Fig. S7) measurements rule out the possibility of other NO<sub>x</sub> impurities in NO gas. As shown by the linear sweep voltammetry (LSV, Fig. 4a), Fe<sub>1</sub>/MoS<sub>2-x</sub> delivers a much higher current density (*j*) in NO-saturated electrolytes than that in Ar-saturated electrolytes beyond an onset potential of  $-0.2$  V, implying the effective NO



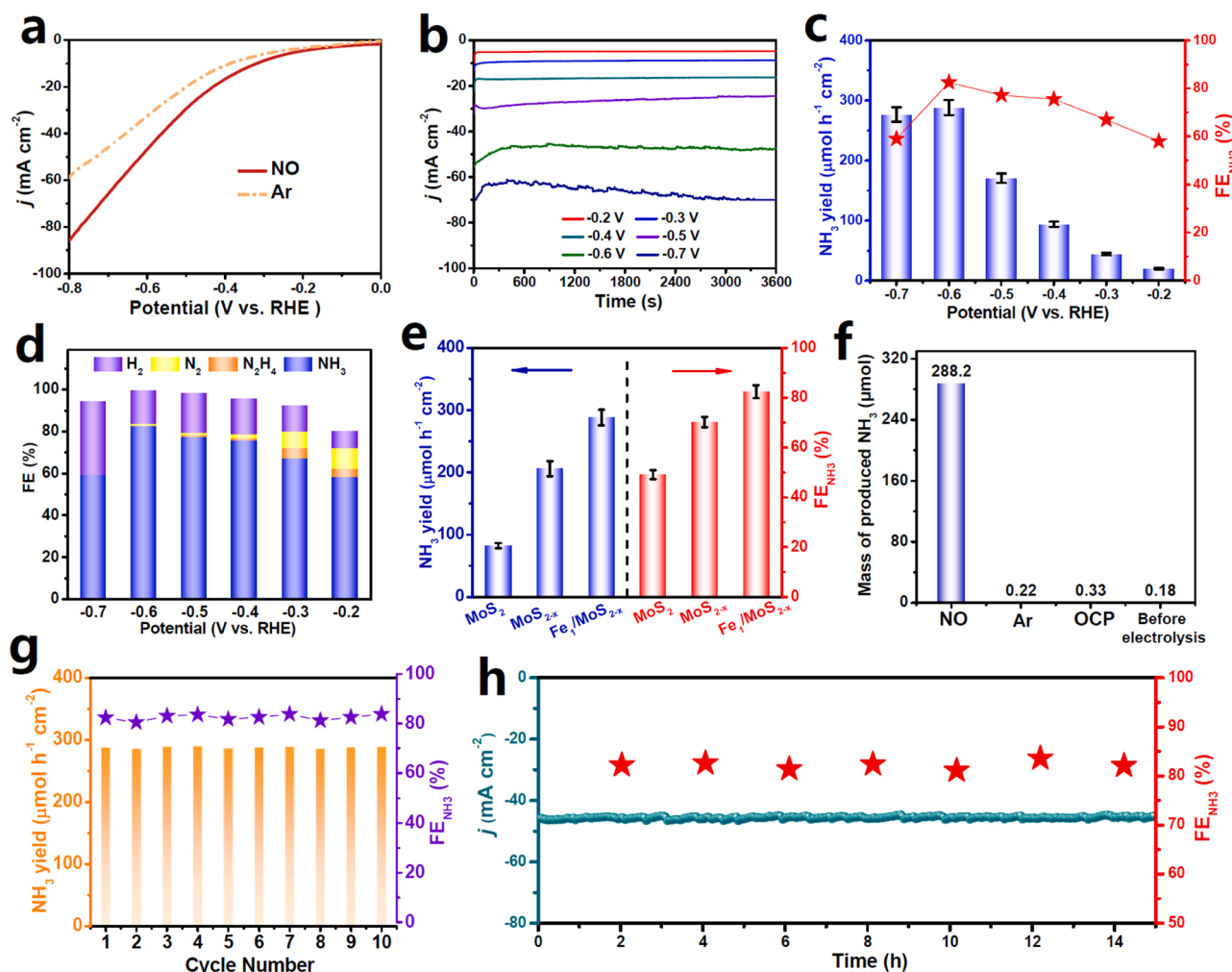


**Fig. 4.** (a) LSV curves of Fe<sub>1</sub>/MoS<sub>2-x</sub> in Ar- and NO-saturated 0.5 M Na<sub>2</sub>SO<sub>4</sub> solution. (b) Chronoamperometry test of Fe<sub>1</sub>/MoS<sub>2-x</sub> at various potentials. (c) FE<sub>NH<sub>3</sub></sub> and corresponding NH<sub>3</sub> yields on Fe<sub>1</sub>/MoS<sub>2-x</sub> at various potentials. (d) FEs of different products. (e) NORR performances of MoS<sub>2</sub>, MoS<sub>2-x</sub>, and Fe<sub>1</sub>/MoS<sub>2-x</sub>. (f) Masses of produced NH<sub>3</sub> on Fe<sub>1</sub>/MoS<sub>2-x</sub> under different conditions. (g) Cycling and (h) long-term tests at -0.6 V.

electroreduction on Fe<sub>1</sub>/MoS<sub>2-x</sub>. The combined chronoamperometric (Fig. 4b) and colorimetric tests (Fig. S8-S10) are then conducted to quantify the NORR performance of Fe<sub>1</sub>/MoS<sub>2-x</sub>. As presented in Fig. 4c, Fe<sub>1</sub>/MoS<sub>2-x</sub> achieves the maximum FE<sub>NH<sub>3</sub></sub> of 82.5% and NH<sub>3</sub> yield of 288.2 μmol h<sup>-1</sup> cm<sup>-2</sup> at -0.6 V, superior to that of most previously reported NORR catalysts (Table S2). The corresponding partial current density at -0.6 V is 38.6 mA cm<sup>-2</sup> (Fig. S11). Meanwhile, Fe<sub>1</sub>/MoS<sub>2-x</sub> presents a significantly higher FE<sub>NH<sub>3</sub></sub> than FE<sub>H<sub>2</sub></sub> and FE<sub>N<sub>2</sub></sub> (Fig. 4d), while its FE<sub>N<sub>2</sub>H<sub>4</sub></sub> is extremely low, suggesting the exceptional NO-to-NH<sub>3</sub> selectivity of Fe<sub>1</sub>/MoS<sub>2-x</sub>.

For comparison, pristine MoS<sub>2</sub> and MoS<sub>2-x</sub> (V<sub>S</sub>-rich but Fe-free) are synthesized (Fig. S12) and their NORR performances are evaluated under the identical conditions. As displayed in Fig. 4e, pristine MoS<sub>2</sub> shows a much inferior performance, whereas sole V<sub>S</sub> introduction (MoS<sub>2-x</sub>) presents a marked performance improvement which can be further enhanced by additionally Fe-doping (Fe<sub>1</sub>/MoS<sub>2-x</sub>). This emphasizes the crucial synergy role of Fe-dopants and V<sub>S</sub> in significantly promoting the NORR activity of Fe<sub>1</sub>/MoS<sub>2-x</sub>. Electrochemical surface area (ECSA, Fig. S13) measurements show that Fe<sub>1</sub>/MoS<sub>2-x</sub> and MoS<sub>2-x</sub> have a comparable ECSA, which is slightly higher than that of pristine MoS<sub>2</sub>, implying that V<sub>S</sub> introduction benefits the increased ECSA [59–61]. Nonetheless, the ECSA-normalized NH<sub>3</sub> yields and FE<sub>NH<sub>3</sub></sub> (Fig. S14) display the quite similar trends with Fig. 4e, revealing that Fe<sub>1</sub>/MoS<sub>2-x</sub> is intrinsically more active than MoS<sub>2</sub> and MoS<sub>2-x</sub>. Additionally, as shown in Fig. S15, Fe<sub>1</sub>/MoS<sub>2-x</sub> and MoS<sub>2-x</sub> both exhibit a

reduced charge transfer resistance relative to pristine MoS<sub>2</sub>, which is ascribed to the synergetic role of Fe-dopants and V<sub>S</sub> to tune the electronic structures of MoS<sub>2</sub> with the improved conductivity, consistent with the DFT results (Figs. 3f and S5).

We then identify the NH<sub>3</sub> source during the electrolysis tests. As present in Fig. 4f, The Ar and open circuit potential (OCP) controls show the negligible detection of NH<sub>3</sub>. Besides, the NO/Ar switching tests reveal that the remarkable NH<sub>3</sub> is only generated in NO-cycles whereas Ar-cycles show almost no detection of NH<sub>3</sub> (Fig. S16). Further, upon using <sup>15</sup>NO feeding gas, <sup>1</sup>H NMR spectra show a doublet coupling peak, very close to that of the standard <sup>15</sup>NH<sub>4</sub><sup>+</sup> sample (Fig. S17). All these results undoubtedly corroborate that the generated NH<sub>3</sub> originates from the NORR rather than the inference of external pollution.

We finally assess the NORR stability of Fe<sub>1</sub>/MoS<sub>2-x</sub>. Fig. 4g shows that both NH<sub>3</sub> yields and FE<sub>NH<sub>3</sub></sub> exhibit little change for the consecutive ten electrolysis cycles, implying the high cycling durability of Fe<sub>1</sub>/MoS<sub>2-x</sub>. Fig. 4h shows a negligible  $j$  decay and small fluctuated FE<sub>NH<sub>3</sub></sub> over 30 h of continuous electrolysis, implying the excellent long-term stability of Fe<sub>1</sub>/MoS<sub>2-x</sub>. Moreover, the morphology (Fig. S18), crystal structure (Fig. S19), and single-atomic coordination structure (Fig. S20) of Fe<sub>1</sub>/MoS<sub>2-x</sub> are well retained after the stability tests, suggesting the robust structural durability of Fe<sub>1</sub>/MoS<sub>2-x</sub>.

### 3.4. Theoretical analysis of NORR mechanism

DFT calculations are carried out to further unveil the origin of the enhanced NORR performance of  $\text{Fe}_1/\text{MoS}_{2-x}$ . Three models are established, including pristine  $\text{MoS}_2$ ,  $\text{MoS}_{2-x}$  (containing sole  $\text{V}_\text{S}$ ) and  $\text{Fe}_1/\text{MoS}_{2-x}$  (containing both  $\text{V}_\text{S}$  and Fe-dopant). The NO molecule prefers to adopt an end-on adsorption configuration on  $\text{MoS}_{2-x}$  (Fig. S21) and  $\text{Fe}_1/\text{MoS}_{2-x}$  (Fig. 5a), where  $\ast\text{NO}$  bonds with unsaturated Mo-Mo and Mo-Fe dual sites, respectively. Both show a stronger NO adsorption than pristine  $\text{MoS}_2$ , as evidenced by the more negative adsorption energies

(Figs. 5a, S21) and enhanced  $\ast\text{NO}/\text{active sites}$  orbital hybridization (Fig. S22). In addition, Fe-Mo dual sites on  $\text{Fe}_1/\text{MoS}_{2-x}$  back-donate total 0.16 |e| to  $\ast\text{NO}$  and the N=O bond is largely elongated to 1.244 Å (Fig. 5b), in contrast to those observed on Mo-Mo dual sites of  $\text{MoS}_{2-x}$  (0.10 |e|, 1.226 Å, Fig. 5c), indicating the further enhanced NO activation on  $\text{Fe}_1/\text{MoS}_{2-x}$  relative to Fe-free  $\text{MoS}_{2-x}$  [62–65]. Therefore, the cooperation of Fe-dopant and  $\text{V}_\text{S}$  enables the creation of Fe-Mo dual sites that can jointly facilitate the NO absorption and activation, beneficial for the subsequent NORR process. Intriguingly, the charge density difference plot (Fig. 5d) reveals the occurrence of both electron

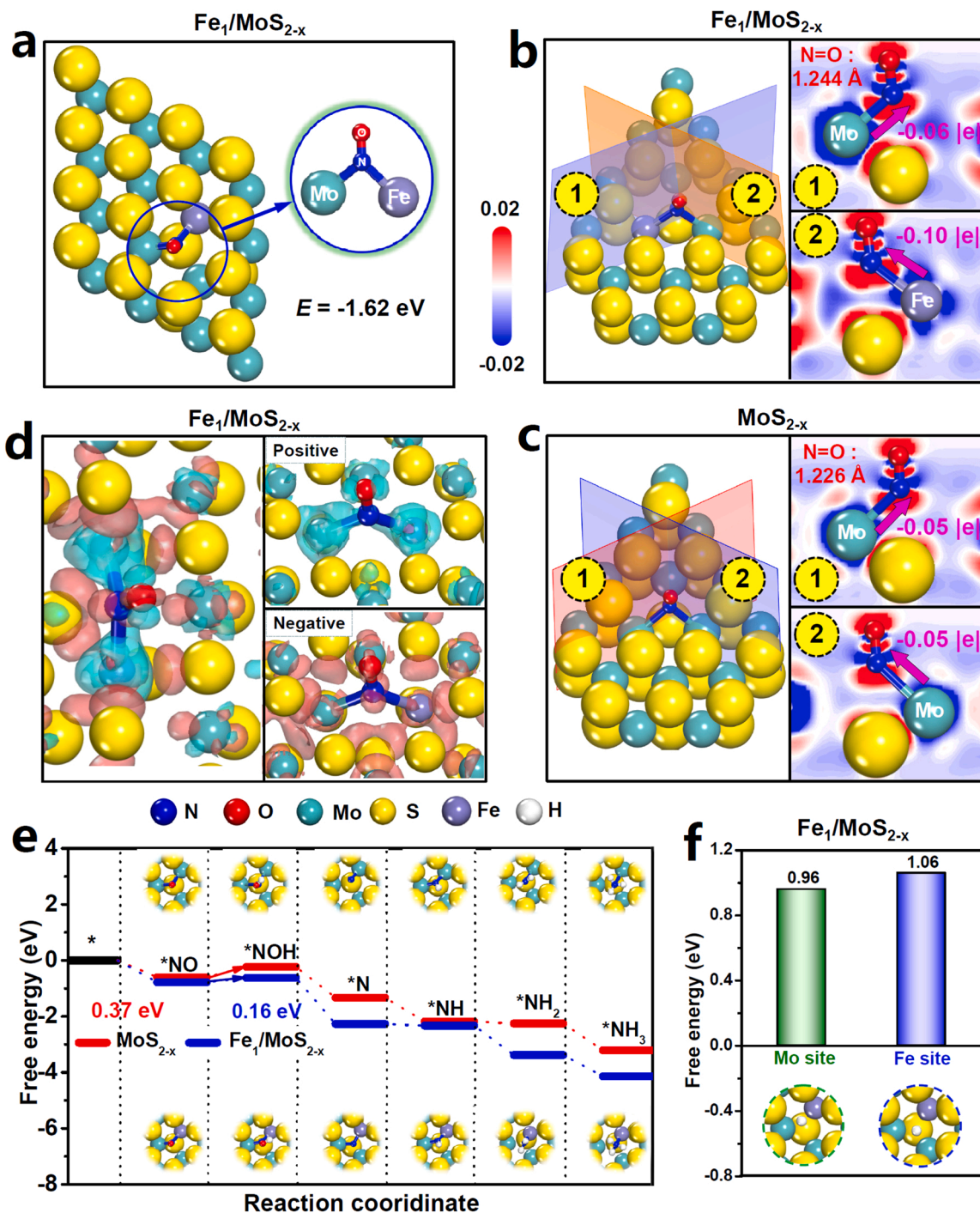


**Fig. 5.** (a) Optimized configuration of NO adsorption on  $\text{Fe}_1/\text{MoS}_{2-x}$  and corresponding adsorption energy ( $E$ ). (b, c) Electron contour maps of NO adsorption on (b)  $\text{MoS}_{2-x}$  and (c)  $\text{Fe}_1/\text{MoS}_{2-x}$ . Blue/red regions represent electron depletion/accumulation. (d) Differential charge density maps of NO adsorption configurations on  $\text{Fe}_1/\text{MoS}_{2-x}$ . Cyan/red regions represent electron depletion/accumulation. (e) Free energy diagrams for NORR on  $\text{MoS}_{2-x}$  and  $\text{Fe}_1/\text{MoS}_{2-x}$ . (f) Free energies of  $\ast\text{H}$  adsorption on  $\text{MoS}_2$  and  $\text{Fe}_1/\text{MoS}_{2-x}$ .

accumulation and depletion around NO, with electron accumulation on the antibonding orbital ( $2\pi^*$ ) and electron depletion on the bonding orbital ( $5\sigma$  and  $1\pi$ ) of NO (Fig. S23), demonstrating the effective NO activation on Fe-Mo dual sites through an electron acceptance-donation mechanism [17].

To further shed light on the enhanced NORR activity of  $\text{Fe}_1/\text{MoS}_{2-x}$ , the free energy profiles are explored (Figs. 5e, S24) [33]. The rate-determining step (RDS) for both  $\text{MoS}_{2-x}$  and  $\text{Fe}_1/\text{MoS}_{2-x}$  is the first hydrogenation step ( $^*\text{NO} \rightarrow ^*\text{NOH}$ ), while the RDS energy barrier of  $\text{Fe}_1/\text{MoS}_{2-x}$  is as low as 0.16 eV, which is 0.21 eV lower than that of  $\text{MoS}_{2-x}$ , probably caused by the more efficient NO activation on Fe-Mo dual sites. Meanwhile, the rest hydrogenation steps of  $\text{Fe}_1/\text{MoS}_{2-x}$  are more exothermic relative to  $\text{MoS}_{2-x}$ , which can release more energy facilitating the successive NORR process. Since HER is the competing reaction against NORR [35], we calculate the adsorption free energy of H ( $G^*_\text{H}$ ) to investigate the HER activity of  $\text{Fe}_1/\text{MoS}_{2-x}$ . Fig. 5f shows that Fe-Mo dual sites of  $\text{Fe}_1/\text{MoS}_{2-x}$  show a considerably positive  $G^*_\text{H}$  ( $G^*_\text{H}(\text{Mo}) = 0.96$  eV,  $G^*_\text{H}(\text{Fe}) = 1.06$  eV) [66]. The rather positive  $G^*_\text{H}$  of Fe-Mo dual sites indicates that  $\text{Fe}_1/\text{MoS}_{2-x}$  can effectively retard the initial proton adsorption and hinder the HER, in favor of the NORR selectivity. These results clearly demonstrate that Fe-Mo dual sites created on  $\text{Fe}_1/\text{MoS}_{2-x}$  can synergistically activate NO, promote the protonation energetics and suppress the HER, resulting in the significantly expedited NORR activity and selectivity.

#### 4. Conclusion

In conclusion, both high NORR activity and selectivity are achieved over  $\text{Fe}_1/\text{MoS}_{2-x}$ , attributed to the crucial role of Fe-Mo dual sites to synergistically activate NO, boost the protonation energetics and impede the HER. This work not only provides the in-depth mechanistic understanding of the NORR mechanism from the perspective of dopant-vacancy synergy effect, but also highlights the combined atomic doping/vacancy engineering strategy to develop high-performance NORR catalysts for  $\text{NH}_3$  electrosynthesis.

#### CRedit authorship contribution statement

**Kai Chen:** Investigation, Methodology, Writing – original draft. **Jiixin Wang:** Investigation, Methodology. **Jilong Kang:** Investigation. **Xubin Lu:** Formal analysis, Methodology. **Xiaolin Zhao:** Software, Visualization. **Ke Chu:** Resources, Conceptualization, Funding acquisition, Writing – review & editing.

#### Declaration of Competing Interest

We declare that we have no known competing financial interests or personal relationships that could have appeared to influence the work reported in this paper.

#### Data availability

The authors do not have permission to share data.

#### Acknowledgments

This work is supported by the National Natural Science Foundation of China (52161025) and Natural Science Foundation of Gansu Province (20JR10RA241).

#### Appendix A. Supplementary material

Supplementary data associated with this article can be found in the online version at doi:10.1016/j.apcatb.2022.122241.

#### References

- [1] J. Liang, Q. Liu, A.A. Alshehri, X. Sun, Nano Res. Energy 1 (2022), e9120010.
- [2] K. Tanifuji, Y. Ohki, Chem. Rev. 120 (2020) 5194–5251.
- [3] G. Qing, R. Ghazfar, S.T. Jackowski, F. Habibzadeh, M.M. Ashtiani, C.-P. Chen, M. R. Smith, T.W. Hamann, Chem. Rev. 120 (2020) 5437–5516.
- [4] H. Shen, C. Choi, J. Masa, X. Li, J. Qiu, Y. Jung, Z. Sun, Chem 7 (2021) 1708–1754.
- [5] Z. Du, J. Liang, S. Li, Z. Xu, T. Li, Q. Liu, Y. Luo, F. Zhang, Y. Liu, Q. Kong, X. Shi, B. Tang, A.M. Asiri, B. Li, X. Sun, J. Mater. Chem. A 9 (2021) 13861–13866.
- [6] H. Chen, J. Liang, L. Li, B. Zheng, Z. Feng, Z. Xu, Y. Luo, Q. Liu, X. Shi, Y. Liu, S. Gao, A.M. Asiri, Y. Wang, Q. Kong, X. Sun, ACS Appl. Mater. Interfaces 13 (2021) 41715–41722.
- [7] X. Li, Y. Luo, Q. Li, Y. Guo, K. Chu, J. Mater. Chem. A 9 (2021) 15955–15962.
- [8] Q. Li, J. Wang, Y. Cheng, K. Chu, J. Energy Chem. 54 (2021) 318–322.
- [9] K. Chu, X. Li, Q. Li, Y. Guo, H. Zhang, Small 17 (2021), 2102363.
- [10] X. Zhao, G. Hu, G.F. Chen, H. Zhang, S. Zhang, H. Wang, Adv. Mater. 33 (2021), 2007650.
- [11] K. Chu, Y. Liu, Y. Li, Y. Guo, Y. Tian, ACS Appl. Mater. Interfaces 12 (2020) 7081–7090.
- [12] K. Chu, Y. Liu, Y. Li, H. Zhang, Y. Tian, J. Mater. Chem. A 7 (2019) 4389–4394.
- [13] K. Chu, Y. Liu, Y. Li, J. Wang, H. Zhang, ACS Appl. Mater. Interfaces 11 (2019) 31806–31815.
- [14] Y. Li, H. Wang, C. Priest, S. Li, P. Xu, G. Wu, Adv. Mater. 33 (2021), 2000381.
- [15] J. Long, S. Chen, Y. Zhang, C. Guo, X. Fu, D. Deng, J. Xiao, Angew. Chem. Int. Ed. 59 (2020) 9711–9718.
- [16] J. Liang, P. Liu, Q. Li, T. Li, L. Yue, Y. Luo, Q. Liu, N. Li, B. Tang, A.A. Alshehri, I. Shaker, P.O. Agboola, C. Sun, X. Sun, Angew. Chem. Int. Ed. 61 (2022), e202202087.
- [17] L. Zhang, J. Liang, Y. Wang, T. Mou, Y. Lin, L. Yue, T. Li, Q. Liu, Y. Luo, N. Li, B. Tang, Y. Liu, S. Gao, A.A. Alshehri, X. Guo, D. Ma, X. Sun, Angew. Chem. Int. Ed. 60 (2021) 25263–25268.
- [18] S. Sethuram Markandaram, T. Muthusamy, S. Shanmugam, Adv. Sci. 9 (2022), 2201410.
- [19] B.H. Ko, B. Hase, H. Shin, Y. Zhao, F. Jiao, J. Am. Chem. Soc. 144 (2022) 1258–1266.
- [20] Y. Xiong, Y. Li, S. Wan, Y. Yu, S. Zhang, Q. Zhong, J. Hazard. Mater. 430 (2022), 128451.
- [21] L. Zhang, Q. Zhou, J. Liang, L. Yue, T. Li, Y. Luo, Q. Liu, N. Li, B. Tang, F. Gong, X. Guo, X. Sun, Inorg. Chem. 61 (2022) 8096–8102.
- [22] L. Ouyang, Q. Zhou, J. Liang, L. Zhang, L. Yue, Z. Li, J. Li, Y. Luo, Q. Liu, N. Li, B. Tang, A. Ali Alshehri, F. Gong, X. Sun, J. Colloid Interface Sci. 616 (2022) 261–267.
- [23] Q. Liu, Y. Lin, L. Yue, J. Liang, L. Zhang, T. Li, Y. Luo, M. Liu, J. You, A.A. Alshehri, Q. Kong, X. Sun, Nano Res. 15 (2022) 5032–5037.
- [24] D. Qi, F. Lv, T. Wei, M. Jin, G. Meng, S. Zhang, Q. Liu, W. Liu, D. Ma, M.S. Hamdy, J. Luo, X. Liu, Nano Res. Energy 1 (2022), e9120022.
- [25] G. Meng, T. Wei, W. Liu, W. Li, S. Zhang, W. Liu, Q. Liu, H. Bao, J. Luo, X. Liu, Chem. Commun. 58 (2022) 8097–8100.
- [26] G. Meng, M. Jin, T. Wei, Q. Liu, S. Zhang, X. Peng, J. Luo, X. Liu, Nano Res. 15 (2022) 8890–8896.
- [27] J. Liang, W.-F. Hu, B. Song, T. Mou, L. Zhang, Y. Luo, Q. Liu, A.A. Alshehri, M. S. Hamdy, L.-M. Yang, X. Sun, Inorg. Chem. Front. 9 (2022) 1366–1372.
- [28] J. Liang, H. Chen, T. Mou, L. Zhang, Y. Lin, L. Yue, Y. Luo, Q. Liu, N. Li, A. A. Alshehri, J. Mater. Chem. A 10 (2022) 6454–6462.
- [29] J. Liang, Q. Zhou, T. Mou, H. Chen, L. Yue, Y. Luo, Q. Liu, M.S. Hamdy, A. A. Alshehri, F. Gong, X. Sun, Nano Res. 15 (2022) 4008–4013.
- [30] Z. Li, Z. Ma, J. Liang, Y. Ren, T. Li, S. Xu, Q. Liu, N. Li, B. Tang, Y. Liu, S. Gao, A. A. Alshehri, D. Ma, Y. Luo, Q. Wu, X. Sun, Mater. Today Phys. 22 (2022), 100586.
- [31] P. Liu, J. Liang, J. Wang, L. Zhang, J. Li, L. Yue, Y. Ren, T. Li, Y. Luo, N. Li, B. Tang, Q. Liu, A.M. Asiri, Q. Kong, X. Sun, Chem. Commun. 57 (2021) 13562–13565.
- [32] X. Li, G. Zhang, P. Shen, X. Zhao, K. Chu, Inorg. Chem. Front. (2023), https://doi.org/10.1039/D2QI02118H.
- [33] X. Li, K. Chen, X. Lu, D. Ma, K. Chu, Chem. Eng. J. 454 (2023), 140333.
- [34] J. Shi, C. Wang, R. Yang, F. Chen, N. Meng, Y. Yu, B. Zhang, Sci. China Chem. 64 (2021) 1493–1497.
- [35] Y. Xiao, C. Shen, Small 17 (2021), 2100776.
- [36] P. Shen, G. Wang, K. Chen, J. Kang, D. Ma, K. Chu, J. Colloid Interface Sci. 629 (2023) 563–570.
- [37] P. Shen, X. Li, Y. Luo, Y. Guo, X. Zhao, K. Chu, ACS Nano 16 (2022) 7915–7925.
- [38] Y. Luo, Q. Li, Y. Tian, Y. Liu, K. Chu, J. Mater. Chem. A 10 (2022) 1742–1749.
- [39] Y. Luo, P. Shen, X. Li, Y. Guo, K. Chu, Nano Res 15 (2022) 3991–3999.
- [40] Y. Luo, K. Chen, P. Shen, X. Li, X. Li, Y. Li, K. Chu, J. Colloid Interface Sci. 629 (2023) 950–957.
- [41] K. Chu, J. Wang, Y. Liu, Q. Li, Y. Guo, J. Mater. Chem. A 8 (2020) 7117–7124.
- [42] K. Chu, Y. Liu, Y. Li, Y. Guo, Y. Tian, H. Zhang, Appl. Catal. B 264 (2020), 118525.
- [43] X. Li, P. Shen, Y. Luo, Y. Li, Y. Guo, H. Zhang, K. Chu, Angew. Chem. Int. Ed. 134 (2022), e202205923.
- [44] Z.-Y. Wu, M. Karamad, X. Yong, Q. Huang, D.A. Cullen, P. Zhu, C. Xia, Q. Xiao, M. Shakouri, F.-Y. Chen, J.Y. Kim, Y. Xia, K. Heck, Y. Hu, M.S. Wong, Q. Li, I. Gates, S. Siahrostami, H. Wang, Nat. Commun. 12 (2021) 2870.
- [45] Z. Fang, Z. Jin, S. Tang, P. Li, P. Wu, G. Yu, ACS Nano 16 (2022) 1072–1081.
- [46] X. Li, T. Li, Y. Ma, Q. Wei, W. Qiu, H. Guo, X. Shi, P. Zhang, A.M. Asiri, L. Chen, B. Tang, X. Sun, Adv. Energy Mater. 8 (2018), 1801357.
- [47] J. Li, Y. Zhang, C. Liu, L. Zheng, E. Petit, K. Qi, Y. Zhang, H. Wu, W. Wang, A. Tiberj, X. Wang, M. Chhowalla, L. Lajunnie, R. Yu, D. Voirey, Adv. Funct. Mater. 32 (2022), 2108316.



- [48] H. Su, L. Chen, Y. Chen, R. Si, Y. Wu, X. Wu, Z. Geng, W. Zhang, J. Zeng, *Angew. Chem. Int. Ed.* 132 (2020) 20591–20596.
- [49] J.-Y. Xue, F.-L. Li, Z.-Y. Zhao, C. Li, C.-Y. Ni, H.-W. Gu, D.J. Young, J.-P. Lang, *Inorg. Chem.* 58 (2019) 11202–11209.
- [50] F.-F. Zhang, C.-Q. Cheng, J.-Q. Wang, L. Shang, Y. Feng, Y. Zhang, J. Mao, Q.-J. Guo, Y.-M. Xie, C.-K. Dong, *ACS Energy Lett.* 6 (2021) 1588–1595.
- [51] H. Su, L. Chen, Y. Chen, Y. Wu, X. Wu, R. Si, W. Zhang, Z. Geng, J. Zeng, *Angew. Chem. Int. Ed.* 132 (2020) 20591–20596.
- [52] W. Liu, J. Feng, T. Wei, Q. Liu, S. Zhang, Y. Luo, J. Luo, X. Liu, *Nano Res.* (2022), <https://doi.org/10.1007/s12274-022-4929-7>.
- [53] S. Gao, T. Wei, J. Sun, Q. Liu, D. Ma, W. Liu, S. Zhang, J. Luo, X. Liu, *Small Struct.* (2022), <https://doi.org/10.1002/ssr.202200086>.
- [54] S. Gao, T. Wang, M. Jin, S. Zhang, Q. Liu, G. Hu, H. Yang, J. Luo, X. Liu, *Sci. China Mater.* (2022), <https://doi.org/10.1007/s40843-022-2236-8>.
- [55] P. Shen, X. Li, Y. Luo, N. Zhang, X. Zhao, K. Chu, *Appl. Catal. B* 316 (2022), 121651.
- [56] G. Wang, P. Shen, Y. Luo, X. Li, X. Li, K. Chu, *Dalton Trans.* 51 (2022) 9206–9212.
- [57] K. Chen, Y. Luo, P. Shen, X. Liu, X. Li, X. Li, K. Chu, *Dalton Trans.* 51 (2022) 10343–10350.
- [58] K. Chu, Y. Luo, P. Shen, X. Li, Q. Li, Y. Guo, *Adv. Energy Mater.* 12 (2022), 2103022.
- [59] L. Zhang, J. Liang, L. Yue, K. Dong, J. Li, D. Zhao, Z. Li, S. Sun, Y. Luo, Q. Liu, C. Guanwei, A. Ali Alshehri, X. Guo, X. Sun, *Nano Res. Energy* 1 (2022), e9120028.
- [60] J. Safaei, G. Wang, *Nano Res. Energy* 1 (2022), e9120008.
- [61] G. Feng, J. He, H. Wang, J. Lin, R. Chen, K. Yi, F. Huang, Z. Lin, M. Wang, *Nano Res. Energy* 1 (2022), e9120029.
- [62] G. Zhang, X. Li, P. Shen, Y. Luo, X. Li, K. Chu, *J. Environ. Chem. Eng.* 10 (2022), 108362.
- [63] Q. Li, P. Shen, Y. Tian, X. Li, K. Chu, *J. Colloid Interface Sci.* 606 (2022) 204–212.
- [64] K. Chu, X. Li, Y. Tian, Q. Li, Y. Guo, *Energy Environ. Mater.* 5 (2022) 1303–1309.
- [65] Y. Cheng, X. Li, P. Shen, Y. Guo, K. Chu, *Energy Environ. Mater.* (2022), <https://doi.org/10.1002/eeem2.12268>.
- [66] X. Yao, J. Zhu, H. Wang, K. Yang, Y. Shu, J. He, *Appl. Surf. Sci.* 587 (2022), 152842.